Extended Hubbard corrected tight-binding model for rhombohedral few-layer graphene

Dongkyu Lee,[1, 2] Wooil Yang,[3] Young-Woo Son,[3] and Jeil Jung[1, 2, *]

[1]*Department of Physics, University of Seoul, Seoul 02504, Korea*
[2]*Department of Smart Cities, University of Seoul, Seoul 02504, Korea*
[3]*Korea Institute for Advanced Study, Seoul 02455, Korea*

(Dated: March 4, 2024)

Rhombohedral multilayer graphene (RnG) featuring partially flat bands has emerged as an important platform to probe strong Coulomb correlation effects. Theoretical consideration of local electron-electron interactions are of particular importance for electronic eigenstates with a tendency to spatially localize. We present a method to incorporate mean-field electron-electron interaction corrections in the tight-binding hopping parameters of the band Hamiltonian within the extended Hubbard model that incorporates *ab initio* estimates of on-site (U) and inter-site (V) Hubbard interactions for the π bands of RnG. Our Coulomb-interaction renormalized band structures feature electron-hole asymmetry, band flatness, band gap, and anti-ferromagnetic ground states in excellent agreement with available experiments for $n \geq 4$. We reinterpret the putative gaps proposed in $n = 3$ systems in terms of shifting electron and hole density of states peaks depending on the range of the Coulomb interaction models.

I. INTRODUCTION

Nearly flat bands confined within a small energy range that are spread in momentum space often lead to localized states in real space. To elucidate the characteristics of flat bands, it is imperative to incorporate local interactions. The eigenstates of flat bands, known as compact localized states, exhibit values only within a finite range [1]. Notable examples of the states include the AA region of magic-angle twisted bilayer graphene (MATBG) [2–4] and the coherent regions of moiré structures of rhombohedral multilayer graphene on hexagonal boron nitride [5–8] and the A sublattice of the first layer with its symmetric counterpart B sublattice of the last layer in rhombohedral stacked n-layer graphene (**RnG**) which has partially flat bands [9–11]. Owing to their localized nature, flat-band materials exhibit heightened sensitivity to variations in local interactions, leading to notable alterations in band flatness, band gap, correlation phase, and beyond [10, 12–14]. On the other hand, outcomes derived from calculations employing the local density approximation (LDA) [15] and generalized gradient approximation (GGA) [16] functional, which neglect local interactions, run the risk of predicting physics that deviate from the actual properties of flat-band materials.

Recent experimental observations have underscored the need for more sophisticated calculations in flatband materials. The reported many-body phenomena in flatband, such as quantum anomalous Hall effect, unconventional superconductivity, and charge density wave [6, 17–20], stem from symmetry breaking induced by external perturbations such as (proximity) spin-orbit coupling and gating. As the properties are dictated by the ratio of external parameters to hopping parameters, an accurate hopping model that incorporates the appropriate interaction strength would effectively mitigate computational complexity and bolster result reliability.

However, a proper model explaining flat band experiments has yet to be proposed, particularly for rhombohedral stacked n-layer graphene (RnG for $n = 3, 4, \cdots$) which has partially flat bands near the high-symmetry points K and K'. The rhombohedral stacked 3-layer graphene (ABC stacked graphene, R3G) exhibits band gap ranging from 0 to 42 meV [21–25]. The estimated Hubbard U value is $4.8t$ from the 42 meV gap where t is the nearest-neighbor hopping parameter [25]. This value significantly surpasses the U value $3.5t$ from the constrained random phase approximation (cRPA) [26] and even the anti-ferromagnetic critical value of monolayer graphene $2.2t$ [27]. On the computational front, gapless states were obtained for all RnG within the GGA [28]. Despite the PBE0 hybrid functional adequately estimating the gapped states with a 39 meV band gap for R3G [9], it faltered in predicting experimental gaps of 10 meV for ABCA stacked graphene (R4G) [10, 29]. Consequently, an appropriate interaction model capable of elucidating experimental results for RnG remains unproposed.

In this paper, we propose realistic extended Hubbard corrected tight-binding models (TB+U+V) for RnG ($n = 1, 2, \cdots, 8$), and discuss their ground states and flat band structures under neutral conditions. The model incorporates three extended Hubbard parameters (U, V_1, V_2) from a newly developed self-consistent density functional theory [30, 31] and hopping parameters obtained from the π-band maximally localized Wannier functions. The local interaction corrected hopping parameters provide a Fermi velocity that matches experimental values well, in contrast to LDA functional density functional theory (DFT) which underestimates it [32, 33]. The ground states of the TB+U+V Hamiltonian accurately predict the particle-hole asymmetry, antiferromagnetic
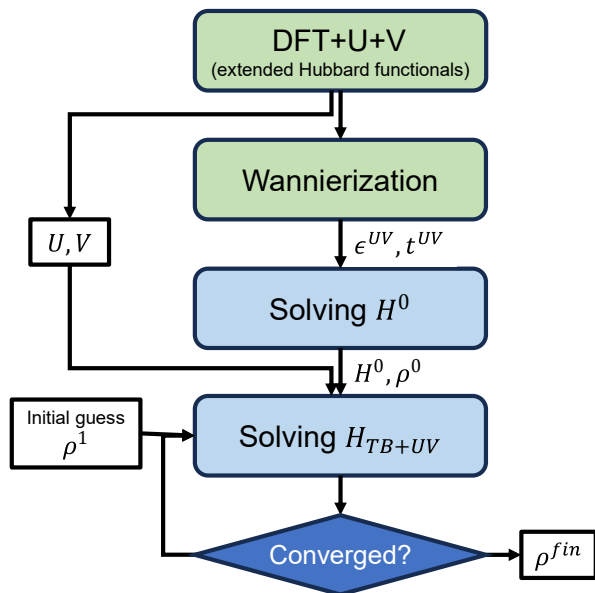
* jeiljung@uos.ac.kr

FIG. 1. A flowchart diagram summarizing the construction and solution process of the TB+U+V model. Hopping coefficients extracted from DFT+U+V include contributions from extended Hubbard interactions. The additional step to calculate ρ^0 is introduced to correct the interaction. The degrees of freedom associated with U and V are eliminated using the extended Hubbard functional method.

band gap, flat bandwidth, and critical temperature for $n \geq 4$. It also provides a new interpretation of the experimental gapped states in R3G, explaining the variations in measured band gap size depending on substrate condition. We expect that these models, being self-consistently determined without empirical variables, will reduce computational complexity and enhance result reliability, in subsequent calculations involving external variables.

II. EXTENDED HUBBARD CORRECTED TIGHT-BINDING MODEL

A. Interacting correction

The physics of interacting models emerges from the competition between hopping parameters and interactions, while effective hopping parameters are renormalized by interactions [34]. Since parameters obtained from DFT are renormalized hopping parameters, careful definition and subtraction of the interaction are necessary to avoid double counting. However, an issue arises when using the LDA functional, as it does not provide information about the magnitude of interactions for the Wannier function basis. Therefore, we turned our attention to DFT+U+V functional [35]. Since the electron-electron interaction potential is restricted to the extended Hubbard interaction, the onsite potential ϵ^{UV} and the hopping parameters t^{UV} extracted from the DFT+U+V can

be defined as follows:

$$\epsilon_i^{UV} \sim \epsilon_{i\sigma} + U_i \rho_{i\tilde{\sigma}}^0 + \sum_j V_{ij} \rho_j^0 \tag{1}$$

$$t_{ij}^{UV} \sim t_{ij\sigma} - V_{ij} \rho_{ij\sigma}^0 \tag{2}$$

where the $\epsilon_{i\sigma}$ and the $t_{ij\sigma}$ are the non-interacting tight-binding parameters between the orbitals i and j of spin σ, the $\tilde{\sigma}$ denotes the opposite spin of σ, the U_i and the V_{ij} are the extended Hubbard parameters which were used in the DFT+U+V calculation, and the ρ^0 is a mean-field density matrix ($\rho_{ij\sigma} = \langle c_{j\sigma}^\dagger c_{i\sigma} \rangle$) obtained from the non-corrected Hamiltonian,

$$H^0 = \sum_{i\sigma} \epsilon_i^{UV} c_{i\sigma}^\dagger c_{i\sigma} + \sum_{ij\sigma} t_{ij}^{UV} c_{i\sigma}^\dagger c_{j\sigma}. \tag{3}$$

Here, we have abbreviated the notation for the density matrix by denoting $\rho_{i\sigma} = \rho_{ii\sigma}$ and $\rho_i = \rho_{i\uparrow} + \rho_{i\downarrow}$ removing the indices.

The interaction correction involves excluding the original electron-electron interaction from the Hamiltonian and introducing a new one based on the updated density matrix. In other words, the interaction corrected Hamiltonian used in the $(N + 1)$th step, where the density matrix obtained from the Nth self-consistent iteration step is ρ^N, is given by,

$$H_{TB+UV}^{(N+1)}(\rho^N) = H^0 + H^{UV}(\rho^N - \rho^0) \tag{4}$$

where the extended Hubbard correction,

$$H^{UV}(\Delta\rho) = \sum_{i\sigma}(U_i \Delta\rho_{i\tilde{\sigma}} + \sum_j V_{ij} \Delta\rho_j) c_{i\sigma}^\dagger c_{i\sigma}$$
$$- \sum_{ij\sigma} V_{ij} \Delta\rho_{ij\sigma} c_{i\sigma}^\dagger c_{j\sigma}.$$

Here, the non-collinear interaction has been ignored.

In typical DFT approaches with Hubbard interactions [36, 37], the determination of the parameters relies on empirical fitting procedures. Recently, however, there have been significant developments in computing those parameters *ab initio* [30, 38–49]. Among them, we used a newly developed first-principles method [30, 31] for on-site and intersite Hubbard interactions by incorporating the Agapito–Curtarolo–Buongiorno Nardelli (ACBN0) pseudohybrid functional for on-site Coulomb interactions [45]. The present method turns out to be very efficient and accurate in obtaining various physical parameters such as bands gaps, atomic forces, phonon dispersions and magnetic moments of correlated solids [30, 31, 48, 50]. Moreover, this method can self-consistently determine the strength of inter-site Hubbard interactions between a pair of orbitals with arbitrary spatial range to handle long-ranged correlations in low dimensional solids [30]. Therefore, our TB+U+V method differs from typical mean-field Hubbard model calculations [51, 52] in that the long-ranged Hubbard parameters can be determined self-consistently and that a step

TABLE I. Calculated extended Hubbard parameters and extracted Dirac velocity of monolayer graphene (R1G) in the DFT+U+V step. We compare our results with those in other methods. The Hubbard parameters are given in eV

	This work	ref[a]	ref[b]	ref[c]
U	6.20	7.56	10.16	-
V_1	3.22	4.02	5.68	-
V_2	2.09	2.57	4.06	-
v_{f} [$10^6 m/s$]	1.09	1.43	-	0.84
t_{eff} [eV]	3.40	4.46	-	2.58

[a] Extended Hubbard functional DFT+U+V [48]
[b] cRPA [53]
[c] LDA [32]

to solve tight-binding Hamiltonian of H^0 is added subsequently. We note that this approach also helps prevent the double-counting of interactions and enhances accuracy significantly. Fig. 1 shows a diagram explaining the process of constructing and solving the H_{TB+UV}.

B. Rhombohedral stacked N-layer graphene

We applied the TB+U+V models for RnG which have partially flat bands. We have considered rigid structures of which the in-plain lattice constant is $a = 2.46$ Å and the interlayer distance is $c = 3.35$ Å in this work. Fig. 2(a) illustrates the unit cell of rhombohedral stacked graphene. DFT calculations were performed with modified QUANTUM ESPRESSO [30, 31, 54] for the extended Hubbard functional DFT+U+V. We used a projector augmented wave (PAW) [55] LDA pseudopotential parameterized by Perdew and Zunger [56] in PSLIBRARY [57]. The Brillouin zone integrations in this step were performed with $60 \times 60 \times 1$ Monkhorst-Pack mesh points. The extended Hubbard correction considered interaction range up to 2.46 Å, including interactions with the second-nearest neighbor orbitals. The onsite parameter U, nearest inter-sublattice parameter V_1, and nearest intra-sublattice parameter V_2 were self-consistently determined for this interaction range. Since there was no significant difference in these Hubbard parameters depending on layer, sublattice, or structure, the same values were used for all basis and every RnG. The non-corrected tight-binding parameters ϵ^{UV} and t^{UV} were obtained by constructing the maximally localized Wannier functions (MLWF) for π-bands of the DFT+U+V calculations. The Wannierization was performed using WANNIER90. The obtained hopping parameters were truncated for use in a model called the F2G2 model [58], which considers up to second-nearest hopping for each sublattice relation as illustrated in Fig. 2(b). The hoppings between the basis differing by three or more layers were excluded, as they were negligible in magnitude. The F2G2 hopping parameters and the non-corrected electronic structure for RnG are explained in Appendix A.

Table I summarizes the parameters obtained during the DFT+U+V step. Our Hubbard parameters show smaller values compared to other references. Due to π-bonding, the π-band orbitals exhibit a broader spread compared to the p_z orbital, and this spread is calculated to increase with the density of the reciprocal space grid [32]. As the spread of orbitals increases, it reduces the magnitude of local interactions. Hence, our results yield smaller values compared not only to cRPA but also to the same extended Hubbard functional DFT+U+V method. The Fermi velocity v_{f} obtained using the slope of the Dirac cone in the monolayer graphene (R1G) confirms a higher value compared to the velocity obtained within the LDA [32, 58], and our value is in good agreement with the experimental value [59]. Furthermore, the effective hopping value t_{eff} calculated numerically from the Fermi velocity also shows improvement over the LDA calculation.

The final step in constructing the TB+U+V Hamiltonian for RnG involved solving the H^0, which includes the F2G2 hopping parameters, to obtain ρ^0. (The energy dispersions near K point of the non-corrected Hamiltonians can be found in Fig. A.1.) During the self-consistent TB+U+V Hamiltonian calculation, a partially dense k-point sampling was employed to prevent overweighted Dirac points, as illustrated in Fig. 2(c). This approach involves creating a coarse grid of dimensions $N_{\mathrm{coarse}} \times N_{\mathrm{coarse}} \times 1$ across the entire Brillouin zone (BZ) and replacing the representative zone at the K point with a dense grid of dimensions $N_{\mathrm{dense}} \times N_{\mathrm{dense}} \times 1$. In this paper, we used $N_{\mathrm{coarse}} = 24$ and $N_{\mathrm{dense}} = 64$, resulting in an effective k-grid density of $1536 \times 1536 \times 1$ near the Dirac points. The density matrix was mixed using the modified Broyden algorithm [60], and iterations were continued until the distance between the vectors of the steps was below 10^{-6}.

III. REALISTIC GAPPED STATES AND FLATBANDS

To validate our model, we compare the self-consistent states of RnG under the neutral state with experimental results. Fig. 3 present the electronic dispersions and the density of states (DOS) near the Dirac K valley of the RnG for ($n \leq 8$). Including unremarkable gapless states in R1G and R2G, we observed a gapless state in R3G and gapped states for $n \geq 4$. In all RnG, the electron pocket (see left insets of the band structures) exhibits a 3-fold rotation symmetry spreading from K to M direction. The hole pocket (right insets of the band structures) appears at the zone boundary of $K \rightarrow M$ for $n \leq 5$. On the other hand from R6G onward, they appear in the $K \rightarrow \Gamma$ direction, displaying strong electron-hole asymmetry along with changes in bandwidth.

We first examined the flat bandwidth W for quantitative analysis, as shown in Fig. 3(b). We used the standard deviation σ of fitted Gaussian functions to calculate the
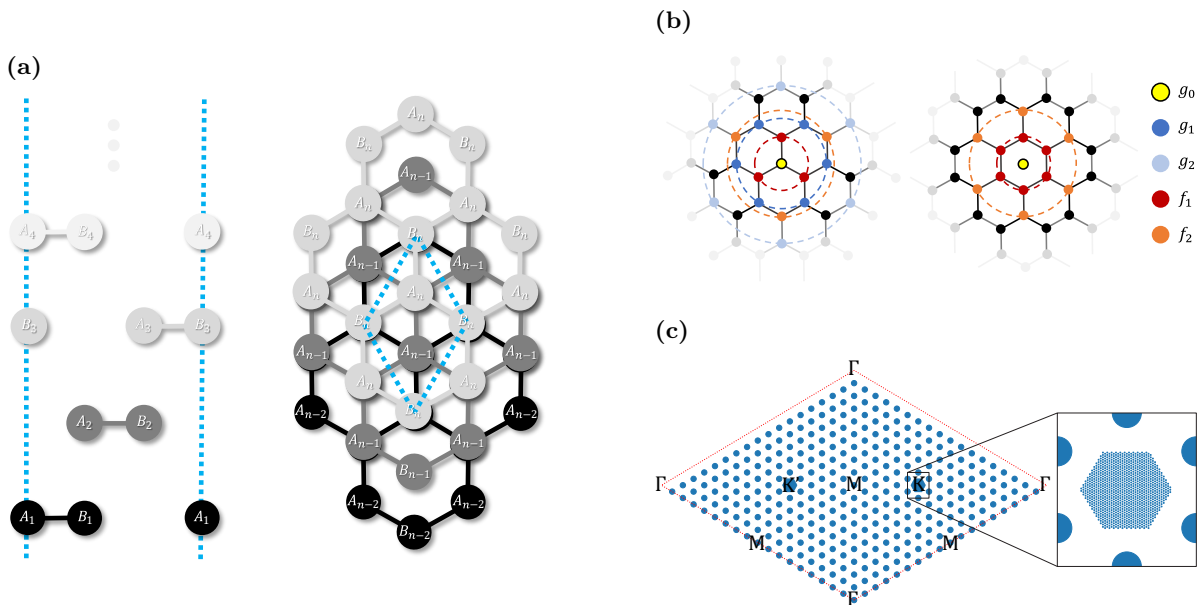
FIG. 2. (a) Schematic sideview(left) and topview(right) of rhombohedral stacked few-layer graphene structure. The label A_i or B_i ($i = 1, 2, \cdots, n$) represents the A or B sublattice orbital of the i-th layer. The dashed lines denote the unit cell of the RnG. (b) Relation classification for F2G2 truncation relative to a central reference position(yellow circle). The F2G2 model truncates hopping parameters up to the second-nearest orbital for the non-zero in-plane displacement between each label. The left panel illustrates the scenario when the in-plain position of the reference orbital is located at the A or B position in the layer, while the right panel depicts the case when it is positioned at the C site. The g_0 represents onsite energy for the same label or perpendicular hopping for different labels. (c) An example of the partially dense k-point sampling used to solve our TB+U+V Hamiltonians of the RnG. The points at $K(K')$ position are replaced by dense grids. The size of each point corresponds to its weight. The illustrated example consists of a 18×18 coarse grid with 32×32 partially dense points resulting in an effective sampling of 576×576 points near the valleys.

width as $W = 2\sqrt{2 \ln 2}\sigma$. The flatness of the conduction band remained nearly constant at around 2 meV for all of the gapped RnG, while the width of the valence band exhibited a linear increase given by

$$W = 1.96n - 6.52 \tag{5}$$

with the stacked layer number n. Our results not only account for the flatness in the experimental results for R4G [10] but also excellently explain the 25 meV bandwidth observed in angle-resolved photoemission spectroscopy (ARPES) measurements for R14G [63]. Additionally, the narrow flat band of about 2 meV widths in R4G and R5G suggests the potential for various many-body phenomena.

Next, we examined the size of the band gap. Two definitions of the band gap are considered in Fig. 3(c). The first is the rigorous definition, the difference between the conduction band minima and valence band maxima, denoted as Δ. The second is the distance between the two peaks in the density of states (DOS), denoted as Δ_{peak}. As observed in the electronic band structure, the band gap emerges for $n \geq 4$. The bandgap Δ increases with the n and converges to 18 meV. Excluding the case of R3G, the Δ_{peak} shows a similar value to the Δ, but due to increasing of the bandwidth of the valence band, there is a trend of a slight deviation from Δ. Our results are in good agreement with a gapless R2G [62] and

the experimental gaps for R4G [10, 29], while previous studies using PBE and PBE0 [9, 61] failed to explain the magnitude of the bandgaps. On the other hand, Our results reveal a gapless state in R3G, whereas experiments suggest various bandgaps spanning from 0 to 42 meV, with most cases indicating finite bandgaps. Specifically, R3G on substrate exhibits gaps ranging from 0.38 to 6 meV [22, 23], while suspended R3G shows either 0 meV [21] or 42 meV [24, 25] in experiments.

Temperature dependence of the band gaps is shown in Fig. 3(d). These calculations were performed by adjusting the temperature values of the Fermi-Dirac distribution in the density matrix integration process. We observed that the RnG ($n \geq 4$), which had gapped ground states, transition to metallic states above certain temperatures. The transition temperatures T_c were determined as the lowest temperature among the results with zero gap. The T_c measured to be 38 K for R4G and 50 K for R5G, increasing with the number of layers and converging to around 65 K. The value of $T_c = 50$ K for R5G is consistent with the experimental result at which the correlated insulator state transitions to a semi-metallic behavior under neutral conditions [64].

We observed the emergence of spin ordering for $n \geq 4$. The spin magnetic moments of the sublattices are illustrated in Fig. 4. The spin magnetic moments for the
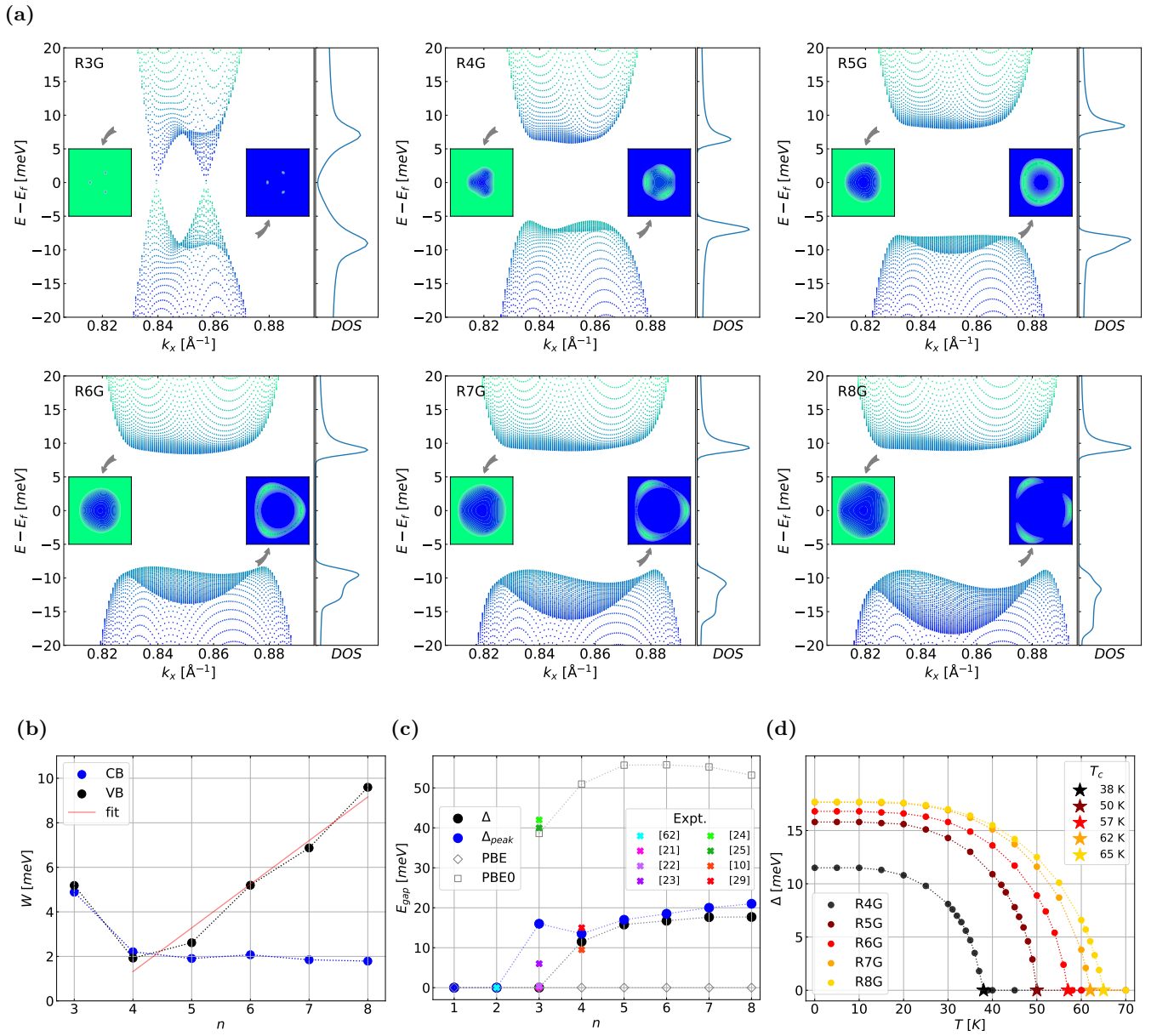
(a)

(b)

(c)

(d)

FIG. 3. (a) TB+U+V band structure and density of states for the ground states of the RnG ($n = 3, 4, \cdots, 8$). The bands show 3D (k_x, k_y, E) electronic dispersions projected to 2D (k_x, E) plane near the K point. The insets of each panel show the contour plots of the conduction band(left insets) and the valence band(right insets). (b) Bandwidths extracted from the peaks of the density of states. The red straight line is obtained using Eq. (5), which is a fitting equation of the valence band flatness for $4 \leq n \leq 8$. (c) Band gaps depending on the number of layers n. The Δ represents the difference between the valence band minima and conduction band maxima, while The Δ_{peak} show the difference in the positions of the two peaks in the density of states. We also list other gaps from PBE(diamond) and PBE0(square) [9, 61]. The cross marks denote experimental band gaps [10, 21–25, 29, 62]. (d) Temperature dependence of the energy gap Δ. The star marks indicate transition temperatures T_c, which represent the lowest temperature points among the data showing zero band gap within an error margin of 1 K.

unlisted sublattices can be obtained by a symmetric relation $\mu_{Ai} = -\mu_{B(n+1-i)}$. The magnetic moments are most large in the surface layer and decrease rapidly with distance from the surface. For a layer index i, A_i and B_i exhibit magnetic moments with differing signs and magnitudes. Consequently, the net spin magnetic moment of the i-th layer is positive for ($i < n/2$) and negative for ($i > n/2$). This indicates that the origin of the gapped ground states is the layer antiferromagnetic (LAF) phase.

Here, we discuss the experimental gapped states in R3G that do not match our results. Contrary to our results indicating the semi-metallic state for R3G, numerous prior experimental studies suggest that the ground state of R3G possesses a bandgap [22–25]. Specifically,
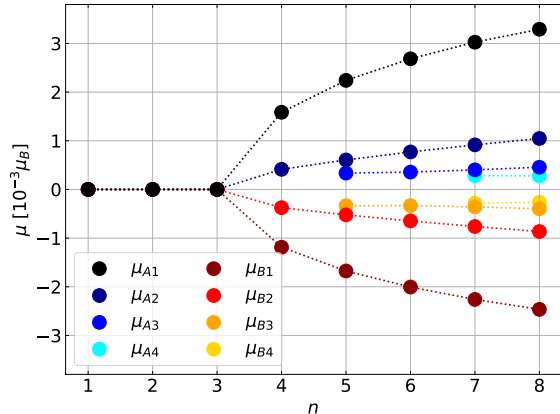
(a)

(b)

FIG. 4. Calculated spin magnetic moments of the sublattices in μ_B. There is a symmetric relation, $\mu_{Ai} = -\mu_{Bn+1-i}$, about the opposite site orbital.
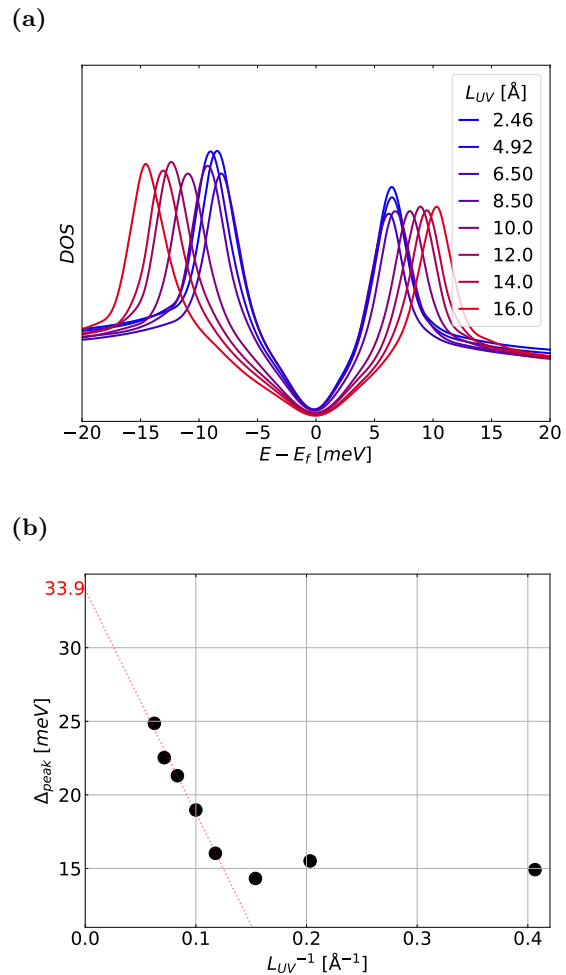
FIG. 5. (a) Comparison of density of states of rhombohedral trilayer graphene for different interaction ranges L_{UV}. Note that the untruncated full hopping parameters were used for this result. (b) Interaction range dependence of the distance between two peaks of the DOS. The red dashed line fitting the data for $L_{UV} \geq 8.5$ exhibits a y-intercept of 33.9 meV.

suspended R3G [24, 25] tends to exhibit a larger bandgap compared to R3G on substrates [22, 23]. However, we have found a clue that can explain the larger and varying bandgaps from our TB+U+V model which includes longer-range interaction. Fig. 5 shows the DOS obtained from our model as the extended Hubbard interaction range L_{UV} is increased. In this calculation, we used the full hopping parameters without F2G2 truncation to assess the effects of long-range interactions. Similar to the divergence in the Fermi velocity observed in monolayer graphene [65], we observed band reshaping in R3G. In our results, the renormalization reduces the DOS near the Fermi level and increases the distance between peaks.

We found that the Δ_{peak} exhibits a linear relationship with L_{UV}^{-1} for $L_{UV} \geq 8.5$, where 8.5 is greater than the distance involving a interaction between A_1 and B_3. Through a finite-size scaling as shown in Fig. 5(b), we obtained a y-intercept of 33.9 meV. It can be confirmed that long-range interactions can increase the Δ_{peak} to a value similar to the size of the experimental gap in the suspended R3G. This suggests that the reduced DOS could lead to the Δ_{peak} being measured as a bandgap. This hypothesis can also explain why the band gap observed for the R3G on substrate is smaller than in suspended R3G. If the range of interaction is reduced due to substrate screening, the DOS near the Fermi level could be measurable. While the 42 meV antiferromagnetic gap would require an excessively large U [24], our model demonstrates that the the band gap size can be explained within realistic interaction strength.

IV. CONCLUSION

In this paper, we introduced the TB+U+V model, a self-consistent tight-binding model that incorporates the mean-field electron-electron interaction correction. We

have applied our model to RnG ($n = 1, 2, \cdots, 8$), reporting the model parameters and the ground states in neutral conditions. We confirmed that using the extended Hubbard functional DFT+U+V yields reasonable interaction parameters and energy dispersions whose Fermi velocity was closer to experiments than other methods [32, 48, 53]. The neutral ground states from the extended Hubbard corrected tight-binding Hamiltonian for RnG reported the semi-metallic phases for $n \leq 3$ and the LAF gapped phases for $n \geq 4$. Our results achieved excellent agreements between their electron-hole asymmetry, bandwidth, bandgap, and transition temperature, and those from experiments for RnG. Lastly, we observed the changes in the DOS near the Fermi level and the distance between the peaks due to the renormalization of the Fermi velocity when adjusting the interaction range in the R3G model. From this observation, we claim the hypothesis that the experimental gap in R3G may be the

distance between the DOS peaks, not a real gap. This hypothesis allowed us to explain the origin and the difference in the experimental band gaps in R3G without the unnaturally large interaction.

In conclusion, we have confirmed that our model can describe naturalistic flat band physics using self-consistently determined interaction parameters. The absence of empirical variables in the model construction step suggests that our method can be easily extended to other flat band materials. Moreover, the determined interaction parameters raise expectations for effectively reducing computational complexity in extended calcula-

tions that consider external perturbations. Hence, we expect that our method may overcome the difficulties of exploring many-body phenomena of flat-band materials.

ACKNOWLEDGMENTS

[1] J.-W. Rhim and B.-J. Yang, Advances in Physics: X **6**, 1901606 (2021).

[2] Y. Choi, J. Kemmer, Y. Peng, A. Thomson, H. Arora, R. Polski, Y. Zhang, H. Ren, J. Alicea, G. Refael, F. von Oppen, K. Watanabe, T. Taniguchi, and S. Nadj-Perge, Nature Physics **15**, 1174 (2019).

[3] M. Koshino, N. F. Yuan, T. Koretsune, M. Ochi, K. Kuroki, and L. Fu, Physical Review X **8**, 031087 (2018).

[4] A. Kerelsky, L. J. McGilly, D. M. Kennes, L. Xian, M. Yankowitz, S. Chen, K. Watanabe, T. Taniguchi, J. Hone, C. Dean, A. Rubio, and A. N. Pasupathy, Nature **572**, 95 (2019).

[5] G. Chen, L. Jiang, S. Wu, B. Lyu, H. Li, B. L. Chittari, K. Watanabe, T. Taniguchi, Z. Shi, J. Jung, Y. Zhang, and F. Wang, Nature Physics **15**, 237 (2019).

[6] G. Chen, A. L. Sharpe, P. Gallagher, I. T. Rosen, E. J. Fox, L. Jiang, B. Lyu, H. Li, K. Watanabe, T. Taniguchi, J. Jung, Z. Shi, D. Goldhaber-Gordon, Y. Zhang, and F. Wang, Nature **572**, 215 (2019).

[7] D. A. G. González, B. L. Chittari, Y. Park, J.-H. Sun, and J. Jung, Physical Review B **103**, 165112 (2021).

[8] Y. Park, Y. Kim, B. L. Chittari, and J. Jung, Physical Review B **108**, 155406 (2023).

[9] B. Pamuk, J. Baima, F. Mauri, and M. Calandra, Physical Review B **95**, 075422 (2017).

[10] A. Kerelsky, C. Rubio-Verdú, L. Xian, D. M. Kennes, D. Halbertal, N. Finney, L. Song, S. Turkel, L. Wang, K. Watanabe, T. Taniguchi, J. Hone, C. Dean, D. N. Basov, A. Rubio, and A. N. Pasupathy, Proceedings of the National Academy of Sciences **118**, e2017366118 (2021).

[11] I. Hagymási, M. S. Mohd Isa, Z. Tajkov, K. Márity, L. Oroszlány, J. Koltai, A. Alassaf, P. Kun, K. Kandrai, A. Pálinkás, P. Vancsó, L. Tapasztó, and P. Nemes-Incze, Science Advances **8**, eabo6879 (2022).

[12] F. Guinea and N. R. Walet, Proceedings of the National Academy of Sciences **115**, 13174 (2018).

[13] J. Vahedi, R. Peters, A. Missaoui, A. Honecker, and G. Trambly de Laissardière, SciPost Physics **11**, 083 (2021).

[14] J. González and T. Stauber, Physical Review B **104**, 115110 (2021).

[15] W. Kohn and L. J. Sham, Physical Review **140**, A1133 (1965).

[16] J. P. Perdew, K. Burke, and M. Ernzerhof, Physical Review Letters **77**, 3865 (1996).

[17] Y. Cao, V. Fatemi, S. Fang, K. Watanabe, T. Taniguchi, E. Kaxiras, and P. Jarillo-Herrero, Nature **556**, 43 (2018).

[18] S. Bhowmik, B. Ghawri, N. Leconte, S. Appalakonda-iah, M. Pandey, P. S. Mahapatra, D. Lee, K. Watanabe, T. Taniguchi, J. Jung, A. Ghosh, and U. Chandni, Nature Physics **18**, 639 (2022).

[19] C.-C. Tseng, X. Ma, Z. Liu, K. Watanabe, T. Taniguchi, J.-H. Chu, and M. Yankowitz, Nature Physics **18**, 1038 (2022).

[20] T. Han, Z. Lu, Y. Yao, J. Yang, J. Seo, C. Yoon, K. Watanabe, T. Taniguchi, L. Fu, F. Zhang, and L. Ju, arXiv:2310.17483 [cond-mat] (2023).

[21] T. Khodkov, I. Khrapach, M. F. Craciun, and S. Russo, Nano Letters **15**, 4429 (2015).

[22] H. J. Van Elferen, A. Veligura, N. Tombros, E. V. Kurganova, B. J. Van Wees, J. C. Maan, and U. Zeitler, Physical Review B **88**, 121302 (2013).

[23] W. Bao, L. Jing, J. Velasco, Y. Lee, G. Liu, D. Tran, B. Standley, M. Aykol, S. B. Cronin, D. Smirnov, M. Koshino, E. McCann, M. Bockrath, and C. N. Lau, Nature Physics **7**, 948 (2011).

[24] Y. Lee, D. Tran, K. Myhro, J. Velasco, N. Gillgren, C. N. Lau, Y. Barlas, J. M. Poumirol, D. Smirnov, and F. Guinea, Nature Communications **5**, 5656 (2014).

[25] Y. Lee, S. Che, J. J. Velasco, X. Gao, Y. Shi, D. Tran, J. Baima, F. Mauri, M. Calandra, M. Bockrath, and C. N. Lau, Nano Letters **22**, 5094 (2022).

[26] T. O. Wehling, E. Şaşıoğlu, C. Friedrich, A. I. Lichten-stein, M. I. Katsnelson, and S. Blügel, Physical Review Letters **106**, 236805 (2011).

[27] S. Sorella and E. Tosatti, Europhysics Letters **19**, 699 (1992).

[28] C. Adamo and V. Barone, The Journal of Chemical Physics **110**, 6158 (1999).

[29] K. Liu, J. Zheng, Y. Sha, B. Lyu, F. Li, Y. Park, Y. Ren, K. Watanabe, T. Taniguchi, J. Jia, W. Luo, Z. Shi, J. Jung, and G. Chen, Nature Nanotechnology , 1 (2023).

[30] S.-H. Lee and Y.-W. Son, Physical Review Research **2**, 043410 (2020).

[31] W. Yang, S.-H. Jhi, S.-H. Lee, and Y.-W. Son, Physical Review B **104**, 104313 (2021).

[32] J. Jung and A. H. MacDonald, Physical Review B **87**,

[33] P. E. Trevisanutto, C. Giorgetti, L. Reining, M. Ladisa, and V. Olevano, Physical Review Letters 101, 226405 (2008).

[34] H.-J. Lee and K.-S. Kim, Physical Review B 97, 155105 (2018).

[35] V. Leiria Campo Jr and M. Cococcioni, Journal of Physics: Condensed Matter 22, 055602 (2010).

[36] V. I. Anisimov, J. Zaanen, and O. K. Andersen, Physical Review B 44, 943 (1991).

[37] V. I. Anisimov, F. Aryasetiawan, and A. I. Lichtenstein, Journal of Physics: Condensed Matter 9, 767 (1997).

[38] H. J. Kulik, M. Cococcioni, D. A. Scherlis, and N. Marzari, Physical Review Letters 97, 103001 (2006).

[39] M. Cococcioni and S. de Gironcoli, Physical Review B 71, 035105 (2005).

[40] T. Miyake and F. Aryasetiawan, Physical Review B 77, 085122 (2008).

[41] T. Miyake, F. Aryasetiawan, and M. Imada, Physical Review B 80, 155134 (2009).

[42] M. Aichhorn, L. Pourovskii, V. Vildosola, M. Ferrero, O. Parcollet, T. Miyake, A. Georges, and S. Biermann, Physical Review B 80, 085101 (2009).

[43] N. J. Mosey and E. A. Carter, Physical Review B 76, 155123 (2007).

[44] N. J. Mosey, P. Liao, and E. A. Carter, The Journal of Chemical Physics 129, 014103 (2008).

[45] L. A. Agapito, S. Curtarolo, and M. Buongiorno Nardelli, Physical Review X 5, 011006 (2015).

[46] N. Tancogne-Dejean, M. J. T. Oliveira, and A. Rubio, Physical Review B 96, 245133 (2017).

[47] I. Timrov, N. Marzari, and M. Cococcioni, Physical Review B 98, 085127 (2018).

[48] N. Tancogne-Dejean and A. Rubio, Physical Review B 102, 155117 (2020).

[49] I. Timrov, N. Marzari, and M. Cococcioni, Physical Review B 103, 045141 (2021).

[50] B. G. Jang, M. Kim, S.-H. Lee, W. Yang, S.-H. Jhi, and Y.-W. Son, Physical Review Letters 130, 136401 (2023).

[51] J. Hubbard, Proceedings of the Royal Society of London. Series A, Mathematical and Physical Sciences 276, 238 (1963).

[52] J. Fernández-Rossier and J. J. Palacios, Physical Review Letters 99, 177204 (2007).

[53] M. Schüler, M. Rösner, T. O. Wehling, A. I. Lichtenstein, and M. I. Katsnelson, Physical Review Letters 111, 036601 (2013).

[54] P. Giannozzi, S. Baroni, N. Bonini, M. Calandra, R. Car, C. Cavazzoni, D. Ceresoli, G. L. Chiarotti, M. Cococcioni, I. Dabo, A. D. Corso, S. d. Gironcoli, S. Fabris, G. Fratesi, R. Gebauer, U. Gerstmann, C. Gougoussis, A. Kokalj, M. Lazzeri, L. Martin-Samos, N. Marzari, F. Mauri, R. Mazzarello, S. Paolini, A. Pasquarello, L. Paulatto, C. Sbraccia, S. Scandolo, G. Sclauzero, A. P. Seitsonen, A. Smogunov, P. Umari, and R. M. Wentzcovitch, Journal of Physics: Condensed Matter 21, 395502 (2009).

[55] P. Blöchl, Physical Review B 50, 17953 (1994).

[56] J. Perdew and A. Zunger, Physical Review B 23, 5048 (1981).

[57] A. Dal Corso, Computational Materials Science 95, 337 (2014).

[58] J. Jung and A. H. MacDonald, Physical Review B 89, 035405 (2014).

[59] C. Hwang, D. A. Siegel, S.-K. Mo, W. Regan, A. Ismach, Y. Zhang, A. Zettl, and A. Lanzara, Scientific Reports 2, 590 (2012).

[60] D. D. Johnson, Physical Review B 38, 12807 (1988).

[61] M. Campetella, J. Baima, N. M. Nguyen, L. Maschio, F. Mauri, and M. Calandra, Physical Review B 101, 165437 (2020).

[62] Y. Zhang, T.-T. Tang, C. Girit, Z. Hao, M. C. Martin, A. Zettl, M. F. Crommie, Y. R. Shen, and F. Wang, Nature 459, 820 (2009).

[63] H. Henck, J. Avila, Z. Ben Aziza, D. Pierucci, J. Baima, B. Pamuk, J. Chaste, D. Utt, M. Bartos, K. Nogajewski, B. A. Piot, M. Orlita, M. Potemski, M. Calandra, M. C. Asensio, F. Mauri, C. Faugeras, and A. Ouerghi, Physical Review B 97, 245421 (2018).

[64] T. Han, Z. Lu, G. Scuri, J. Sung, J. Wang, T. Han, K. Watanabe, T. Taniguchi, H. Park, and L. Ju, Nature Nanotechnology , 1 (2023).

[65] D. C. Elias, R. V. Gorbachev, A. S. Mayorov, S. V. Morozov, A. A. Zhukov, P. Blake, L. A. Ponomarenko, I. V. Grigorieva, K. S. Novoselov, F. Guinea, and A. K. Geim, Nature Physics 7, 701 (2011).

Appendix A: Non-corrected Tight-binding Hamiltonian

In this appendix, we list the F2G2 truncated hopping parameters ϵ^{UV} and t^{UV} for RnG in Table A.1. The Hamiltonian H^0 in Eq. (3) using the hopping parameters exhibits the ground state under neutral conditions in a spin-unpolarized case. Fig. A.1 show the electronic band and DOS of the H^0.

TABLE A.1: F2G2 truncated hopping parameters in eV from the Wannierization step. Two sites in the label column denote the hopping between those sites. Note that inversion symmetry leads to the relations between the labels, $(A_i A_j) \leftrightarrow (B_{n+1-i} B_{n+1-j})$ and $(A_i B_j) \leftrightarrow (B_{n+1-i} A_{n+1-j})$.

RnG	label	g/f	g_0	g_1/f_1	g_2/f_2
R1G	$A_1 A_1$	g	-3.5564	0.2185	0.0521
	$A_1 B_1$	f		-3.7339	-0.1665
R2G	$A_1 A_1$	g	-2.8384	0.2214	0.0512
	$B_1 B_1$	g	-2.8110	0.2133	0.0514
	$A_1 B_1$	f		-3.7396	-0.1629
	$A_1 A_2$	f		0.0848	-0.0311
	$A_1 B_2$	f		0.1308	-0.0692
	$B_1 A_2$	g	0.3328	-0.0055	-0.0008
R3G	$A_1 A_1$	g	-2.0493	0.2219	0.0513
	$B_1 B_1$	g	-2.0247	0.2142	0.0515
	$A_2 A_2$	g	-2.0728	0.2161	0.0493
	$A_1 B_1$	f		-3.7375	-0.1716
	$A_2 B_2$	f		-3.7432	-0.1751
	$A_1 A_2$	f		0.0881	-0.0345
	$A_1 B_2$	f		0.1357	-0.0746
	$A_1 A_3$	f		0.0065	-0.0017
	$A_1 B_3$	g	0.0046	0.0016	-0.0014
	$B_1 A_2$	g	0.3321	-0.0051	-0.0008
	$B_1 B_2$	f		0.0862	-0.0354
				Continued on next table...	

TABLE A.1 (continued)

RnG	label	g/f	g_0	g_1/f_1	g_2/f_2	RnG	label	g/f	g_0	g_1/f_1	g_2/f_2
	B_1A_3	f		0.0068	-0.0058		A_2B_4	g	0.0053	0.0013	-0.0012
	A_1A_1	g	-1.2643	0.2219	0.0522		B_2A_3	g	0.3455	-0.0034	-0.0012
R4G	B_1B_1	g	-1.2384	0.2133	0.0521		B_2B_3	f		0.0863	-0.0310
	A_2A_2	g	-1.2899	0.2147	0.0501		B_2A_4	f		0.0070	-0.0038
	B_2B_2	g	-1.2876	0.2156	0.0503		B_2B_4	f		0.0062	-0.0017
	A_1B_1	f		-3.7361	-0.1616		A_3A_4	f		0.0864	-0.0310
	A_2B_2	f		-3.7417	-0.1615		A_3B_4	f		0.1327	-0.0671
	A_1A_2	f		0.0882	-0.0313		B_3A_4	g	0.3450	-0.0035	-0.0012
	A_1B_2	f		0.1336	-0.0685		A_1A_1	g	-0.0155	0.2251	0.0557
	A_1A_3	f		0.0063	-0.0010	R7G	B_1B_1	g	0.0066	0.2146	0.0554
	A_1B_3	g	0.0052	0.0014	-0.0013		A_2A_2	g	-0.0444	0.2180	0.0540
	B_1A_2	g	0.3415	-0.0045	-0.0012		B_2B_2	g	-0.0449	0.2175	0.0540
	B_1B_2	f		0.0848	-0.0320		A_3A_3	g	-0.0444	0.2177	0.0539
	B_1A_3	f		0.0069	-0.0041		B_3B_3	g	-0.0438	0.2176	0.0539
	B_1B_3	f		0.0061	-0.0012		A_4A_4	g	-0.0442	0.2176	0.0539
	A_2A_3	f		0.0864	-0.0313		A_1B_1	f		-3.7315	-0.1615
	A_2B_3	f		0.1331	-0.0681		A_2B_2	f		-3.7362	-0.1613
	B_2A_3	g	0.3416	-0.0039	-0.0011		A_3B_3	f		-3.7365	-0.1618
	A_1A_1	g	-1.2639	0.2220	0.0522		A_4B_4	f		-3.7365	-0.1618
R5G	B_1B_1	g	-1.2384	0.2133	0.0522		A_1A_2	f		0.0880	-0.0322
	A_2A_2	g	-1.2908	0.2147	0.0500		A_1B_2	f		0.1325	-0.0696
	B_2B_2	g	-1.2869	0.2157	0.0503		A_1A_3	f		0.0061	-0.0022
	A_3A_3	g	-1.2883	0.2150	0.0501		A_1B_3	g	0.0060	0.0013	-0.0013
	A_1B_1	f		-3.7361	-0.1618		B_1A_2	g	0.3461	-0.0036	-0.0012
	A_2B_2	f		-3.7417	-0.1618		B_1B_2	f		0.0856	-0.0320
	A_3B_3	f		-3.7419	-0.1615		B_1A_3	f		0.0071	-0.0030
	A_1A_2	f		0.0883	-0.0313		B_1B_3	f		0.0059	-0.0022
	A_1B_2	f		0.1337	-0.0687		A_2A_3	f		0.0864	-0.0323
	A_1A_3	f		0.0064	-0.0010		A_2B_3	f		0.1316	-0.0694
	A_1B_3	g	0.0051	0.0014	-0.0013		A_2A_4	f		0.0060	-0.0022
	B_1A_2	g	0.3414	-0.0045	-0.0012		A_2B_4	g	0.0058	0.0012	-0.0013
	B_1B_2	f		0.0849	-0.0320		B_2A_3	g	0.3481	-0.0028	-0.0012
	B_1A_3	f		0.0068	-0.0043		B_2B_3	f		0.0864	-0.0321
	B_1B_3	f		0.0062	-0.0010		B_2A_4	f		0.0071	-0.0029
	A_2A_3	f		0.0867	-0.0313		B_2B_4	f		0.0060	-0.0022
	A_2B_3	f		0.1335	-0.0681		A_3A_4	f		0.0863	-0.0323
	A_2A_4	f		0.0063	-0.0009		A_3B_4	f		0.1318	-0.0693
	A_2B_4	g	0.0049	0.0014	-0.0013		A_3A_5	f		0.0060	-0.0022
	B_2A_3	g	0.3416	-0.0040	-0.0012		A_3B_5	g	0.0057	0.0012	-0.0013
	B_2B_3	f		0.0862	-0.0314		B_3A_4	g	0.3483	-0.0028	-0.0013
	B_2A_4	f		0.0069	-0.0041		B_3B_4	f		0.0865	-0.0322
	A_1A_1	g	-0.6406	0.2234	0.0539		B_3A_5	f		0.0071	-0.0029
R6G	B_1B_1	g	-0.6157	0.2139	0.0537		A_1A_1	g	0.6084	0.2265	0.0575
	A_2A_2	g	-0.6671	0.2161	0.0520	R8G	B_1B_1	g	0.6288	0.2155	0.0570
	B_2B_2	g	-0.6662	0.2164	0.0522		A_2A_2	g	0.5789	0.2200	0.0561
	A_3A_3	g	-0.6667	0.2160	0.0520		B_2B_2	g	0.5767	0.2181	0.0558
	B_3B_3	g	-0.6653	0.2163	0.0520		A_3A_3	g	0.5789	0.2190	0.0557
	A_1B_1	f		-3.7340	-0.1611		B_3B_3	g	0.5783	0.2187	0.0555
	A_2B_2	f		-3.7389	-0.1602		A_4A_4	g	0.5783	0.2188	0.0556
	A_3B_3	f		-3.7391	-0.1604		B_4B_4	g	0.5784	0.2188	0.0556
	A_1A_2	f		0.0882	-0.0312		A_1B_1	f		-3.7291	-0.1628
	A_1B_2	f		0.1326	-0.0683		A_2B_2	f		-3.7336	-0.1636
	A_1A_3	f		0.0063	-0.0016		A_3B_3	f		-3.7341	-0.1642
	A_1B_3	g	0.0054	0.0014	-0.0012		A_4B_4	f		-3.7340	-0.1641
	B_1A_2	g	0.3432	-0.0040	-0.0012		A_1A_2	f		0.0872	-0.0333
	B_1B_2	f		0.0845	-0.0316		A_1B_2	f		0.1320	-0.0714
	B_1A_3	f		0.0069	-0.0039		A_1A_3	f		0.0059	-0.0022
	B_1B_3	f		0.0061	-0.0017		A_1B_3	g	0.0066	0.0011	-0.0014
	A_2A_3	f		0.0866	-0.0310		B_1A_2	g	0.3475	-0.0033	-0.0012
	A_2B_3	f		0.1327	-0.0671		B_1B_2	f		0.0871	-0.0323
	A_2A_4	f		0.0061	-0.0017		B_1A_3	f		0.0072	-0.0025

TABLE A.1 (continued)

RnG	label	g/f	g_0	g_1/f_1	g_2/f_2
B_1B_3	f			0.0058	-0.0023
A_2A_3	f			0.0858	-0.0334
A_2B_3	f			0.1298	-0.0723
A_2A_4	f			0.0058	-0.0022
A_2B_4	g	0.0064	0.0011	-0.0014
B_2A_3	g	0.3517	-0.0022	-0.0013
B_2B_3	f			0.0873	-0.0328
B_2A_4	f			0.0073	-0.0025
B_2B_4	f			0.0058	-0.0022
A_3A_4	f			0.0864	-0.0331

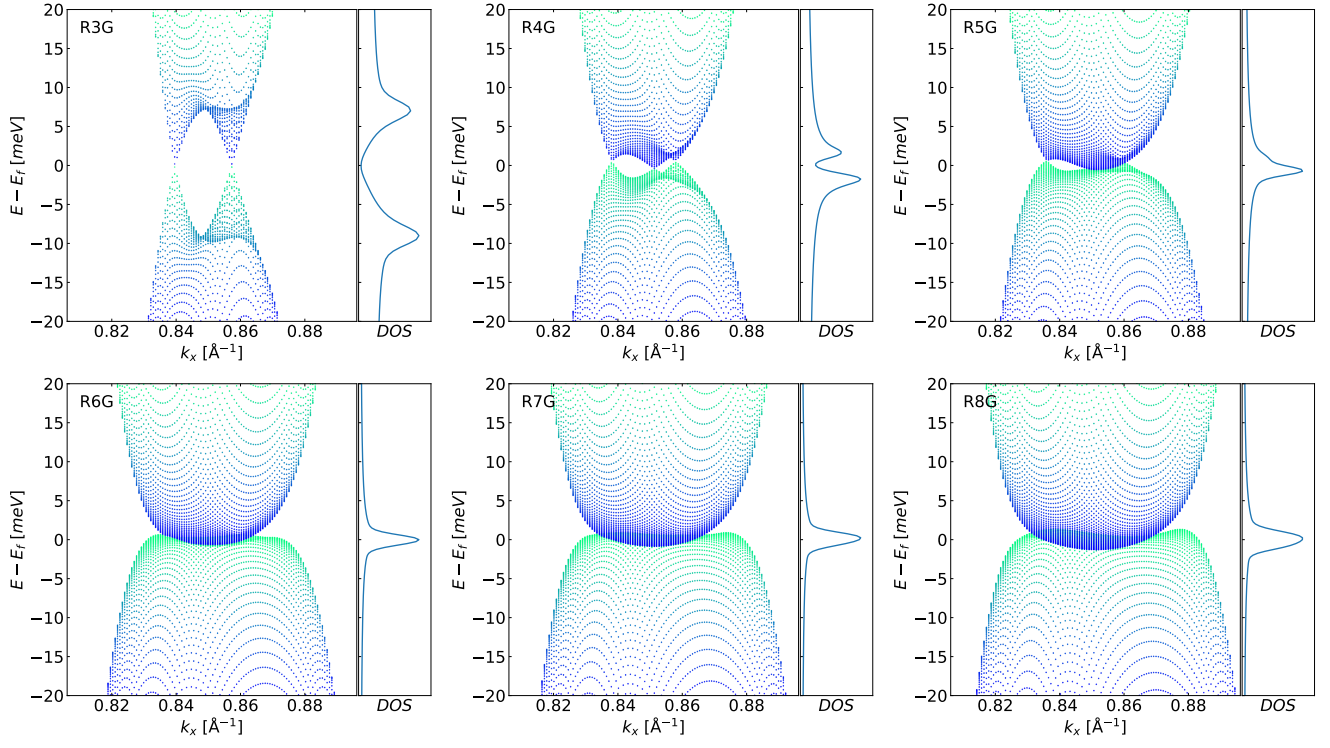| A_3B_4	f			0.1300	-0.0720
A_3A_5	f			0.0059	-0.0022
A_3B_5	g	0.0064	0.0010	-0.0014
B_3A_4	g	0.3519	-0.0022	-0.0014
B_3B_4	f			0.0866	-0.0331
B_3A_5	f			0.0073	-0.0025
B_3B_5	f			0.0059	-0.0022
A_4A_5	f			0.0865	-0.0331
A_4B_5	f			0.1300	-0.0720
B_4A_5	g	0.3518	-0.0022	-0.0014

FIG. A.1. H^0 band structure and density of states for the RnG ($n = 3, 4, \cdots, 8$)